JACS
JOURNAL OF THE AMERICAN CHEMICAL SOCIETY
pubs.acs.org/JACS
Article

Diameter-Controlled Synthesis of Horizontally Aligned Carbon Nanotube Arrays via S-Apphire Interface Engineering

Jianping Wang, Zijian Wang, Chengyu Wang, Shurui Wang, Yue Li, Zhe Liu, Xinyi Cai, Jin Zhang,* Jia Si,* Xiaoxu Zhao,* and Liu Qian*

Cite This: https://doi.org/10.1021/jacs.6c08950
Read Online
ACCESS | Metrics & More | Article Recommendations | Supporting Information

ABSTRACT: Precise control over the size and dispersion of supported metal nanoparticles is a fundamental issue in heterogeneous catalysis, governing both reaction activity and selectivity. However, regulating these parameters remains challenging due to thermodynamically driven sintering, particularly under high-temperature conditions. This challenge is acutely exemplified in the growth of horizontally aligned carbon nanotube (HACNT) arrays, where the catalyst size dictates the CNT diameter, and consequently the electronic properties for integrated circuit applications. Here, we report a deterministic sulfur-modified sapphire (S-apphire) interface engineering strategy to regulate catalyst dispersion and the resulting CNT diameter. We establish cohesive energy (E_{coh}) as a quantitative descriptor of metal−metal versus metal−support interactions and show that sulfur modification selectively tunes E_{coh} to control nanoparticle size predictably. This strategy achieves a diameter reduction to ∼1.26 nm using Ti catalysts, meeting the requirements for the 3 nm technology node of CNT integrated circuits, while preserving high array density and good alignment. Top-gated field-effect transistors fabricated on these arrays exhibit on/off current ratios approaching 10^7, superior to devices with uncontrolled diameters. Beyond CNT electronics, this work offers a generalizable thermodynamic framework for designing stable, size-controlled metal nanostructures via interface engineering.

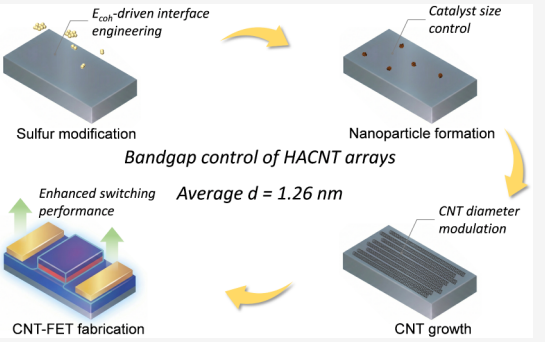

1. INTRODUCTION

Catalyst dispersion is a fundamental issue in heterogeneous catalysis. Across the historical evolution of catalysts from bulk metals to nanoclusters,[1] and more recently to single-atom catalysts (SACs),[2−4] catalyst design has consistently trended toward better dispersion. Nanoscale catalysts present much higher surface-to-volume ratios and more accessible active sites, yielding greatly enhanced catalytic activity.[1,5,6] Fundamentally, catalyst dispersion is a thermodynamically governed process, and the interaction between the catalyst and the support determines whether the catalyst aggregates into large clusters or remains atomically dispersed under operational conditions, particularly at elevated temperatures. This catalyst−support interaction thus provides a rational handle for engineering catalyst size and distribution, offering a general framework for controlling nanoscale structures during high-temperature catalytic processes.[7−9] The synthesis of carbon nanotubes (CNTs) via chemical vapor deposition (CVD) presents a typical and demanding case study of the universal principles. The size and dispersion of the catalyst nanoparticles under a high growth temperature influence both the growth activity and the structure of the CNTs, which are directly related to their application potential.

CNTs have emerged as leading candidates for next-generation semiconductor materials because of their unique one-dimensional structures and excellent electronic properties.[10,11] Field-effect transistors (FETs) based on horizontally aligned CNT (HACNT) arrays have demonstrated performance superior to that of commercial silicon-based FETs with similar gate lengths.[10] Intrinsically, the performance of CNT-based electronics is dictated by the structure of HACNT arrays. In FETs, a properly designed bandgap enables effective switching between on/off logic states,[11,12] and for semiconducting CNTs, controlling the bandgap fundamentally boils down to controlling the CNT diameter, since there is a determined relationship between the CNT bandgap (E_G) and its diameter (d).[13] Current research primarily focuses on increasing the density of HACNT arrays[14,15] or enriching the purity of semiconducting CNTs,[16] which has made CNT-FETs functional but not yet commercially reliable and controllable.

Received: May 9, 2026
Revised: July 9, 2026
Accepted: July 13, 2026

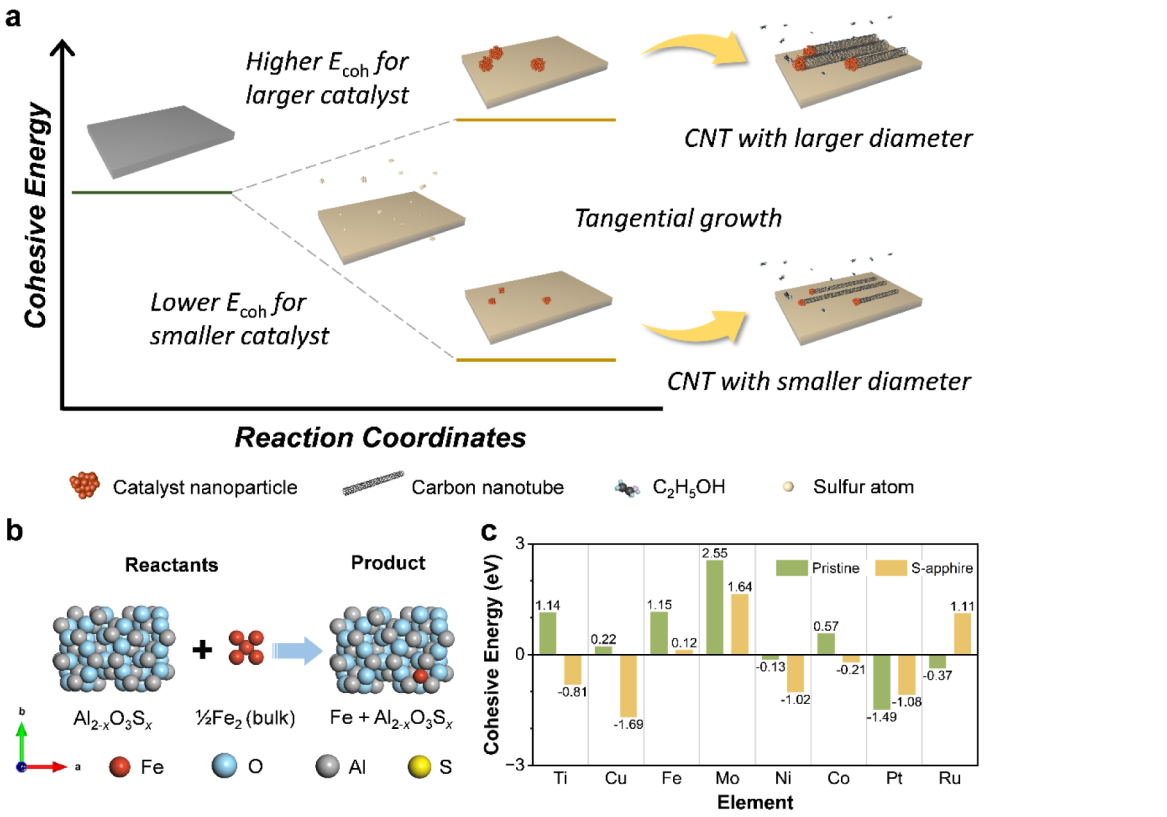

Figure 1. E_{coh}-guided CNT diameter control with S-apphire strategy. (a) Schematic illustration of the relationship between E_{coh}, catalyst nanoparticle size, and CNT diameter upon sulfur modification. Catalysts with larger E_{coh} favor stronger metal−metal cohesion, leading to larger nanoparticles and consequently CNTs with larger diameters, whereas smaller E_{coh} promotes finer nanoparticle dispersion and smaller CNT diameters. (b) Definition of E_{coh} in this work. E_{coh} is defined as the energy difference between the catalyst−support complex and the isolated bulk catalyst and support slab, serving as a thermodynamic descriptor for catalyst dispersion. (c) E_{coh} calculation for different catalysts. The green and yellow bars represent E_{coh} for the pristine and sulfur-modified sapphire, respectively.

However, controlling the diameter of CNTs to tune their band structures is an essential step toward practical applications.

For CNT-FETs, a larger bandgap (smaller diameter) would enable a larger on/off current ratio and allow lower band-to-band leakage currents, enhancing the FET device performance. On the other hand, a smaller diameter also leads to a higher Schottky contact resistance between the CNT and the electrode, limiting the on-state current.[17,18] In contrast, a larger CNT diameter can improve the on-state current but results in a higher off-state current.[17,18] This trade-off collectively sets an optimal CNT diameter of approximately 1.3 nm for CNT-based integrated circuits (ICs).[11]

For most growth systems employing metal catalysts, controlling the diameter of CNTs is essentially governed by controlling the size of the catalyst nanoparticles based on the vapor−liquid−solid (VLS) growth mode.[19] Conventional methods to tune catalyst size, including plasma treatments[20] and variations in catalyst−support combinations,[21,22] often disrupt the density and alignment of HACNT arrays. Given that both liquid catalysts and a-plane sapphire support are indispensable for achieving high-density, well-aligned HACNT arrays,[14,15,23] any viable strategy for diameter control must operate within this constrained growth system. Under these conditions, the catalyst−support interface emerges as the key remaining degree of freedom that can be rationally engineered without compromising the array density or alignment.

Atomic-scale modification of the support provides a powerful route to tailor the interface, and sulfur is particularly suitable for this purpose. Previous studies have shown that sulfur incorporation can strongly stabilize supported metal catalysts under high-temperature conditions, while remaining structurally compatible with crystalline support.[24,25] Moreover, sulfur has been extensively employed in the growth of transition-metal dichalcogenides on sapphire without degrading support crystallinity or epitaxial alignment.[26,27] These considerations suggest that sulfur modification of sapphire can selectively modulate the catalyst−support interaction, thereby regulating catalyst dispersion and nanoparticle size, while preserving the structural integrity required for well-aligned HACNT array growth.

Herein, we developed a sulfur-modified sapphire (S-apphire) strategy to achieve the diameter-controlled synthesis of HACNT arrays by employing cohesive energy (E_{coh}) as a quantitative descriptor. We demonstrate that sulfur modification effectively tunes the catalyst−support interaction, thus regulating nanoparticle size, and enabling precise diameter control while strictly preserving the high density and good alignment of HACNT arrays. Specifically, we successfully achieved targeted diameter control of CNTs catalyzed by Fe, Ti, and Pt nanoparticles. Notably, HACNT arrays grown from the Ti catalyst with the S-apphire strategy yield a diameter distributuion of 1.26 ± 0.22 nm, and FETs fabricated on these arrays achieved exceptional on/off current ratios with highest approaching 10^7. This work establishes a predictive framework linking interface thermodynamics to device-level performance. Moreover, beyond CNT synthesis, this strategy provides a

https://doi.org/10.1021/jacs.6c08950
J. Am. Chem. Soc. XXXX, XXX, XXX−XXX

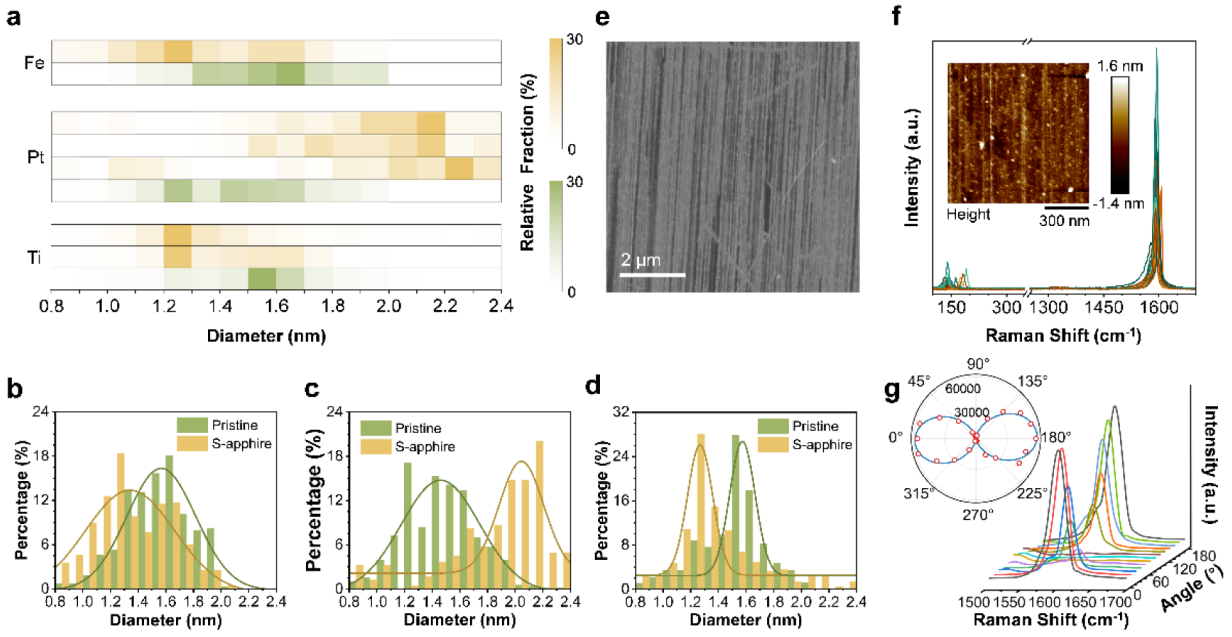

Figure 2. Characterizations of as-grown HACNT arrays. (a) Diameter distribution of HACNT arrays grown from different catalysts, and without and with the S-apphire strategy under different growth conditions. The color intensity represents CNT relative abundance in each diameter bin: green represents samples without the S-apphire strategy, and yellow represents samples with the S-apphire strategy. (b–d) Diameter distribution statistics of HACNT arrays grown from Fe (b), Pt (c), and Ti (d) catalysts. (e) A typical SEM image of HACNT arrays grown from Fe with the S-apphire strategy, showing high density and uniform distribution. (f) Raman line mapping spectra (excited with a 532 nm wavelength laser) of the HACNT arrays. The inset is a typical AFM image. (g) Polarized Raman spectra of the as-grown HACNT arrays, showing good alignment. The inset is a polar plot of Raman G-band intensity as a function of polarization angle.

universal model for rational catalyst design in heterogeneous catalysis, where controlling metal–support interactions is paramount.

2. RESULTS AND DISCUSSION

2.1. The Theoretical Basis of the S-Apphire Interface Engineering Strategy

In the VLS growth of CNTs, the size and dispersion of liquid catalyst nanoparticles are governed by the competition between metal–metal cohesion and metal–support interactions; this competition can be understood as a thermodynamic competition between metal–metal agglomeration (which drives nanoparticle sintering) and metal–support anchoring (which promotes fine dispersion). Cohesive energy (E_{coh}), defined as the energy required to dissociate a metal atom from the bulk to support surface, directly quantifies the outcome of this competition and the intrinsic tendency of a metal to aggregate, as verified in single-atom catalysis.[28,29] Metals with higher E_{coh} favor stronger metal–metal bonding, promoting nanoparticle coalescence and larger size, whereas a more negative E_{coh} signifies that the metal–support interaction overpowers the metal–metal cohesion; consequently, the catalyst atoms are firmly anchored to the support, restricting nanoparticle growth and preserving a highly dispersed state under identical growth conditions.

Within this framework, E_{coh} serves as a descriptor linking catalyst thermodynamics to nanoparticle size. Figure 1a schematically illustrates how the E_{coh} value tunes catalyst size in the S-apphire strategy. It is noteworthy that the thermodynamics of catalyst nanoparticle migration and formation on the support surface is determined by E_{coh}, which is modulated by the S-apphire strategy compared to the pristine support. For catalysts that lead to a lower E_{coh} after sulfur modification, the formation of smaller nanoparticles was promoted, and consequently, CNTs with smaller diameters were favored. In contrast, larger E_{coh} promotes larger catalyst size, leading to CNTs with a larger diameter. To quantitatively understand this mechanism, a rigorous thermodynamic definition of E_{coh} is required.

Figure 1b defines E_{coh} by modeling the reaction starting from a support surface slab and a bulk catalyst crystal, in their thermodynamically stable configurations. Upon adsorption, the final state is modeled using an adatom structure. The catalyst atom loses its metallic bonds in the bulk and forms new bonds with the support. The E_{coh} is defined as

$$E_{coh} = E_{complex} - (E_{surface} + E_{metal})$$

where $E_{complex}$ is the DFT total energy of the support surface slab with a single adsorbed catalyst atom, $E_{surface}$ is the DFT total energy of the bare support surface slab, and E_{metal} is the DFT total energy per atom of the catalyst in its bulk metallic phase; this equation presents the change of total energy for the single-atom formation process. A more negative E_{coh} signifies that bonding with the support is more thermodynamically favored than remaining in the bulk crystal. Consequently, this catalyst would be likely to form a single-atom catalyst, rather than clustering. In general, a smaller (more negative) cohesive energy correlates with superior dispersion. Based on this correlation, E_{coh} can serve as a predictive tool to screen suitable catalysts.

Leveraging this theoretical descriptor to move beyond trial and error, we performed a comprehensive screening of E_{coh} for various commonly used catalysts in HACNT array growth. We first calculated the most stable adsorption site (see Table S1 for details). Results of E_{coh} are shown in Figure 1c (see Methods, Supporting Note 1 and Figure S2 for DFT details).

https://doi.org/10.1021/jacs.6c08950
J. Am. Chem. Soc. XXXX, XXX, XXX–XXX

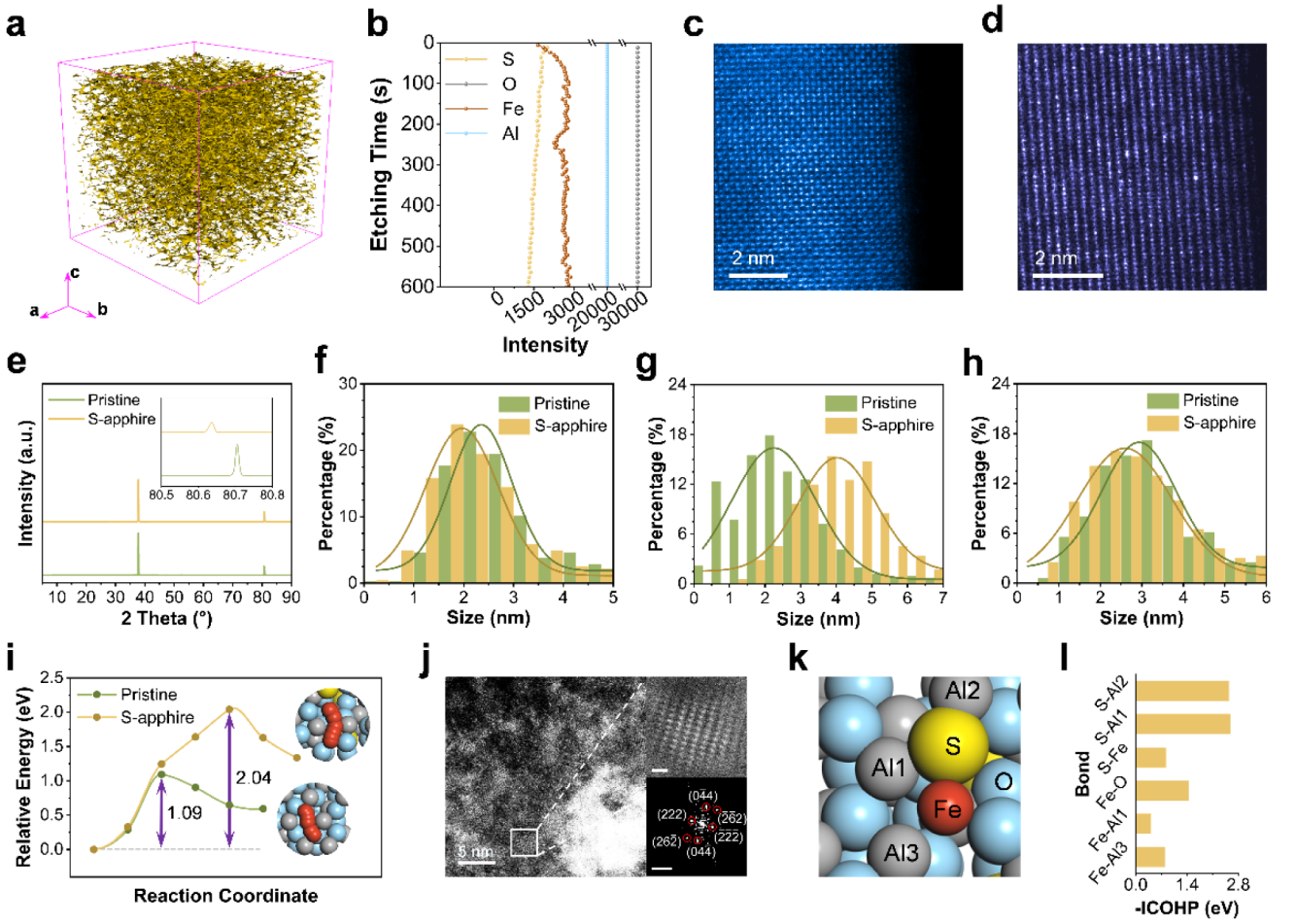

Figure 3. Experimental evidence for sulfur-modified interface engineering and its impact on catalyst nanoparticles. (a) Three-dimensional TOF-SIMS reconstruction of sulfur atoms, showing sulfur distribution in the sapphire support. (b) TOF-SIMS depth profiles of S and Fe concentrations, normalized by O and Al, respectively. (c–d) Cross-sectional atomic-resolution ADF- STEM images showing the preserved Al_2O_3 crystal structure after sulfur modification, along the [1 3 1] (c) and [2 1 0] (d) zone axes. (e) XRD patterns of pristine and sulfur-modified sapphire support; the inset is a detailed scan of the sapphire (2 2 $\bar{4}$ 0) peak. (f–h) Size distributions of Fe (f), Pt (g), and Ti (h) catalyst nanoparticles, respectively, with and without sulfur modification, obtained from AFM images. (i) Calculated surface migration barriers of Fe atoms on pristine and sulfur-modified sapphire surfaces using the CINEB method. (j) SAC-TEM image of a representative Fe catalyst nanoparticle (size of 1.8 nm), with an enlarged atomic-resolution image and corresponding FFT pattern. (k–l) ICOHP analysis model (k) and results (l) of the interaction strengths among sulfur, catalyst, and support atoms, showing that S–Al interaction strength is significantly stronger than S–Fe interaction.

It is evident that sulfur modification decreases E_{coh} for Fe, Ti, and Ni, favoring smaller nanoparticles, while it increases E_{coh} for Pt and Ru. This screening provides a clear guideline for the diameter control strategy and allows us to directly predict the trend of diameter shifts prior to experiments.

2.2. Experimental Validation of Cohesive-Energy-Guided Diameter Control

Guided by the theoretical predictions, we performed experiments to validate the projected diameter shifts and assess the quality of the resulting HACNT arrays. The process started from pristine sapphire, and ion implantation was employed to load catalysts into the sapphire supports. After preprocessing, the supports were placed in a Y-shaped quartz tube (see Methods for information about the catalyst loading and support preprocessing procedure; see Figure S1 for the shape of the Y-shaped tube), which was employed to integrate the sulfur modification and HACNT array growth processes, allowing both steps to occur sequentially within a single experiment. When the temperature was raised to the target value, sulfur was introduced to modify the support. Subsequently, H_2 was introduced to provide a reductive atmosphere, reducing the catalyst and enabling nanoparticle formation. Finally, the carbon source was introduced, leading to the growth of HACNT arrays (see Methods for further details). Figure 2a shows the main results of CNT diameter distribution, grown from different catalysts with or without the S-apphire strategy, and under different growth conditions. Diameter distributions were obtained from line mapping of Raman spectra of three different excitation laser wavelengths,[30−32] to ensure statistical reliability (see Methods, Supporting Note 2, Figures S3–S12 and Table S2 for details and original Raman spectra). The color intensity represents the relative abundance of CNTs in each diameter bin.

As predicted by the E_{coh} calculations, the diameter distributions shifted systematically upon S-apphire strategy. For Fe and Ti, which exhibit lower E_{coh} after sulfur modification, the distributions shift toward smaller diameter. Conversely, for Pt, which has a higher E_{coh} after sulfur modification, the distribution shifts toward a larger diameter. Three representative plots corresponding to Fe, Pt, and Ti are shown in Figure 2b–d, which show that the mean diameter shifts from 1.56 to 1.34 nm for Fe, from 1.57 to 1.26 nm for Ti, and from 1.46 to 2.04 nm for Pt. We further verified the diameter distribution for HACNT arrays grown from Ti and with the S-apphire strategy via atomic force microscope (AFM), the average diameter is 1.24 ± 0.19 nm, showing well consistency with Raman statistics (see Figure S13 for details). All growth conditions were kept identical for each catalyst to isolate the effect of the S-apphire strategy. Notably, the HACNT array with a 1.26 nm diameter achieved by the Ti catalyst meets the

https://doi.org/10.1021/jacs.6c08950
J. Am. Chem. Soc. XXXX, XXX, XXX−XXX

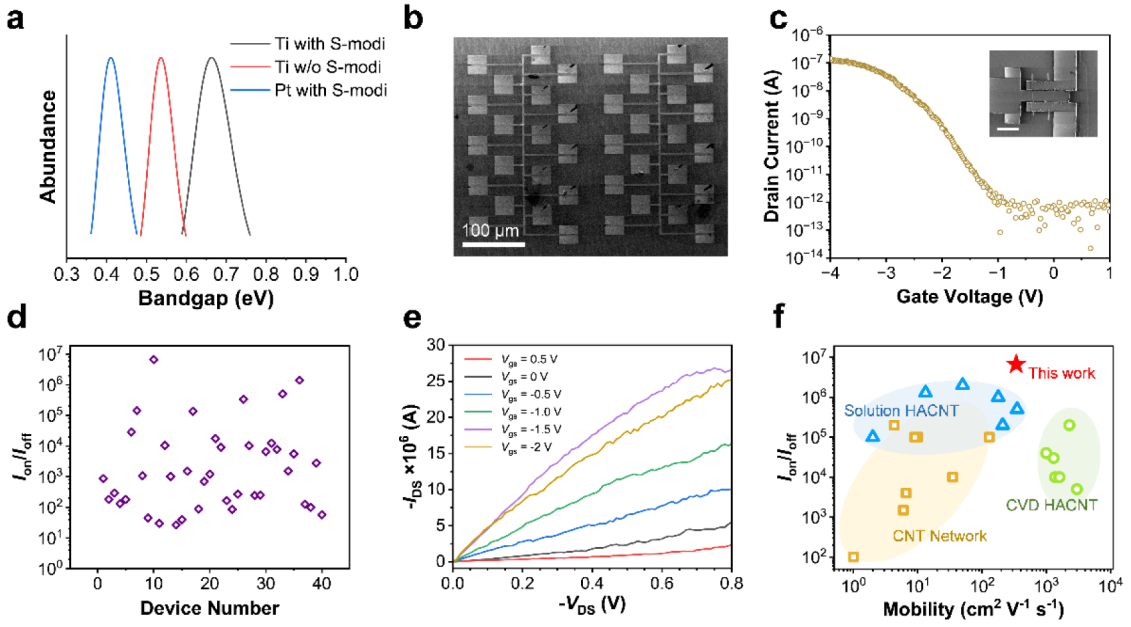

Figure 4. Performances of top-gated FETs based on diameter-controlled HACNT arrays. (a) Calculated bandgap distributions of three representative HACNT array samples, demonstrating effective bandgap modulation in the range of 0.4−0.7 eV. (b) An SEM image of the top-gated CNT-FETs. (c) Transfer characteristics of a representative FET based on HACNT arrays grown with the S-apphire strategy. The inset is the corresponding FET image, scale bar: 2 μm. (d) Statistical distribution of on/off current ratios for the measured CNT-FETs. (e) Output characteristics of a typical CNT-FET device exhibiting a high on/off current ratio. (f) Benchmark of the macroscopic FET performance (mobility versus on/off current ratio) achieved in this work against previously reported CNT-FETs based on random CNT networks, conventional CVD arrays, and solution-assembled arrays.

diameter requirement for the 3 nm technological node in CNT-FET ICs,[11] underscoring the practical potential of the S-apphire strategy. However, it is crucial to confirm that these diameter shifts are intrinsic to the interface engineering.

To address this, we performed control experiments under varying temperatures and flow rates. As shown in Figure 2a, the diameter distributions remained similar across these different experimental conditions for Pt and Ti, robustly confirming that the observed changes were induced by the S-apphire strategy. We further characterized the density, quality, and alignment of the HACNT arrays by scanning electron microscopy (SEM), AFM, and polarized Raman spectra. Figure 2e shows the high density and uniform distribution of the HACNT array grown from Fe catalysts (see Figure S14−S15 for details), quantified to be 15 tubes μm^{-1} via the AFM image inset in Figure 2f. Raman line mapping results of the HACNT array sample showed the G/D band ratio exceeding 100 (Figure 2f), confirming the high quality of the HACNT arrays. Besides, polarized Raman spectra[10] in Figure 2g shows that the HACNT array sample is highly aligned, with a standard deviation of 3.02° (see Methods, Supporting Note 2 for alignment characterizing details). Thus, the S-apphire strategy effectively tunes the diameter of CNTs in agreement with theoretical predictions, while preserving excellent array density, quality, and alignment.

2.3. Experimental Insights into the Mechanism of Diameter Modulation

To understand the physicochemical origin of this effective diameter control, we first verified the successful incorporation of sulfur into the lattice of sapphire. We performed a time-of-flight secondary ion mass spectrometry (TOF-SIMS) test on the samples,[15,33,34] which were prepared in the same procedure but without the carbon supplement. With an etching speed of approximately 0.1 nm per second, mass spectrometry was used to analyze element composition at different depths. Figure 3a is a 3D plot of sulfur distribution, and Figure 3b shows the depth profiles of S and Fe concentrations, normalized by O and Al in negative and positive modes, respectively. TOF-SIMS revealed a uniform distribution of sulfur to a depth of 60 nm, thereby confirming the effective incorporation of the sulfur modification. Furthermore, the measured Al/S ratio of approximately 10:1 was consistent with that of the DFT model.

Since the presence of sulfur was confirmed, we next investigated whether this modification compromised the atomic structure of the sapphire support by transmission electron microscopy (TEM) and X-ray diffraction (XRD). A focused ion beam (FIB) was used to obtain the cross-sectional sample of the sulfur-modified support surface (see Supporting Note 3 for details), which was then applied for spherical-aberration-corrected TEM (SAC-TEM) characterization (see Methods for details). Atomic-resolution annular dark field-scanning TEM (ADF-STEM) images along two different directions in Figure 3c−d indicate that the crystal structure of Al_2O_3 was preserved after sulfur modification.[35] Figure S16 shows the electron energy loss spectroscopy (EELS) profile, showing the trace existence of sulfur in the support surface. Figure 3e shows the XRD patterns of sapphire support with and without sulfur modification. The (2 2 $\bar{4}$ 0) peak shift in the image inset originates from a measurable shift in the lattice parameter after the introduction of S, consistent with the DFT result. Besides, no impurity phases appear after sulfur modification, explaining the retained alignment capability of the substrate for HACNT growth shown in Figure 2g. Both TEM and XRD results demonstrate the excellent defect tolerance of the sapphire support. This structural tolerance is consistent with the nature of sapphire (corundum), which can accommodate various dopants, for instance, ruby is essentially sapphire doped with Cr^{3+}.[36,37] Furthermore, the X-ray photoelectron spectroscopy (XPS) image in Figure S17 shows that sulfur in S-apphire lattice is in the +6 oxidation state. We propose that sulfur substitutes for Al to achieve this oxidation state,[38,39] which is supported by Bader charge analysis (see Methods and Figure S18) indicating electron loss upon substitution. Furthermore, comprehensive experimental controls and thermodynamic calculations unequivocally rule out the formation of surface sulfates, confirming that sulfur is deeply incorporated via lattice substitution (see Supporting Note 4 and Figure S17 for detailed discussions).

Given that the surface electronic landscape has been modified by sulfur modification, it is expected that the wetting and aggregation

https://doi.org/10.1021/jacs.6c08950
J. Am. Chem. Soc. XXXX, XXX, XXX−XXX

behaviors of metal nanoparticles will be fundamentally altered. AFM was employed to study the size shift of the catalyst nanoparticles (see Figure S19 for AFM images). Figure 3f–h shows the nanoparticle size distribution for Fe, Pt, and Ti, respectively, whose size distribution shifts are in accordance with E_{coh} prediction in Figure 1c after sulfur modification. By fitting the distributions with a Gaussian function, it was observed that Fe and Ti nanoparticles became smaller from an average of 2.35 to 1.97 nm and 2.93 to 2.59 nm, respectively, and in contrast, the average size of Pt nanoparticles increased from 2.25 to 4.02 nm after sulfur modification. To further elucidate the mechanism behind the size shift, climbing image nudged elastic band (CINEB) calculation was employed to study the surface diffusion barrier of Fe atoms before and after sulfur modification (see Methods for details). As shown in Figure 3i, a larger diffusion barrier was observed after sulfur modification; this higher barrier inhibited the coalescence and migration of Fe atoms, thereby suppressing the formation of larger nanoparticles and leading to the observed finer size distribution.[24]

Furthermore, we analyzed the composition of the catalyst nanoparticles to rule out any impact of surface sulfur on their structure and properties. The nanoparticles were transferred from the S-apphire support to a Cu grid by a PMMA-assisted method (see Methods and Supporting Note 5 for details). Figure 3j shows a TEM image of catalyst nanoparticles with an enlarged high-resolution TEM (HRTEM) image of a nanoparticle with a size of 1.8 nm, a typical size suitable for CNT growth. The fast Fourier transform (FFT) pattern of this nanoparticle fits well with Fe_2O_3 (see Table S3 for details), without sulfur incorporation.[40] It is important to emphasize that this oxide is a postgrowth passivation phase resulting from ambient air exposure during sample transfer. As thoroughly verified by thermodynamic analyses and *in situ* literature,[41] the active catalyst nanoparticles remain in a fully reduced, highly dynamic liquid-like metallic state during the CVD process (see Supporting Note 6 for details). This result is further confirmed by the analysis of another nanoparticle shown in Figure S20 (see Table S4 for details). Furthermore, EDS mapping of a larger nanoparticle indicates an atomic Fe:O ratio of approximately 2:3 with a negligible sulfur signal (see Figure S21 and Table S5 for details). We also constructed a model to quantify the interaction strength between the surface sulfur atom, catalyst, and support, as shown in Figure 3k and l (see details in Figure S22 and Tables S6–S7). The interaction strength of the sulfur atom with Al at the support surface is much stronger than with Fe, indicating that the sulfur modification targets the support, rather than the catalysts. Consequently, sulfur remains thermodynamically locked in the support lattice, modulating the cohesive energy without compromising the intrinsic structure and functions of the catalyst nanoparticles.

2.4. Device-Level Implications of Deterministic CNT Diameter Control

The deterministic control over the CNT diameter achieved by the S-apphire strategy directly translates into tunable electronic structures. To quantify this, we evaluated the bandgap engineering capabilities of our method by calculating three representative HACNT array samples[13] (Figure 4a). The data reveal a broad yet controlled distribution of bandgaps ranging from 0.4 to 0.7 eV. This result confirms that our approach enables the precise modulation of nanotube electronic properties, establishing the material foundation for optimizing IC applications.

Translating this bandgap engineering capability into practical device performances, we fabricated 40 top-gated FETs using HACNT arrays with a precisely controlled diameter of 1.26 nm. The device structure is shown in Figure 4b (see fabrication details in Methods). Theoretically, reducing the CNT diameter increases the bandgap, which is expected to suppress ambipolar transport and enhance gate modulation in FETs. Consistent with this physical expectation, the transfer characteristics and on/off current ratio statistics shown in Figure 4c,d and Figure S23 demonstrate good switching performance, representing the favorable regime of small CNT diameters. Specifically, the FETs achieve on/off current ratios approaching 10^7, and the proportion of devices with a ratio exceeding 10^4 is greater than 25%. The significance of this diameter control becomes evident when comparing these results to a baseline using larger-diameter tubes. To establish a control-variable relationship, we take previous work[15] with CNT diameters around 1.5 nm as baseline devices, which were synthesized and fabricated using the exact same CVD growth parameters and identical device fabrication processes, with the sole exception being the absence of the sulfur modification. The devices without sulfur modification reported a maximum on/off current ratio of 10^5, with merely 10% of devices exceeding 10^4 (see Supporting Note 7 and Figure S24 for more comparisons). This performance gap provides compelling evidence that the S-apphire strategy yields a higher proportion of small-diameter CNTs with larger bandgaps, thereby validating the critical link between diameter, bandgap, and switching efficiency. Figure 4e further presents representative output characteristics (V_{gs} from 0.5 to −2 V), confirming well-defined FET operation without distinct Schottky barriers.

To place these results in a broader context, we benchmarked the performance of our devices against state-of-the-art CNT-FETs reported in the literature (Figure 4f, see detailed data in Table S8). Historically, achieving both high mobility and high switching capability in CNT-FETs has presented a severe trade-off.[42] By leveraging diameter-dependent bandgap modulation to enhance the on/off current ratio while preserving HACNT array quality for high carrier mobility, the S-apphire strategy enables our devices to break the long-standing performance trade-off in CNT-FETs, achieving an outstanding on/off current ratio approaching 10^7 alongside highly competitive mobility.

3. CONCLUSION

In conclusion, we developed a deterministic and generalizable S-apphire strategy for controlling the diameter of CNTs, a key structural parameter governing their electronic properties. By establishing E_{coh} as a descriptor for catalyst dispersion and by engineering the catalyst–support interface through sulfur modification, CNT diameter can be predictably tuned at the synthesis level while preserving high density and good alignment. Via the S-apphire strategy, we successfully obtained HACNT arrays with an average diameter reduced to 1.26 nm using Ti catalysts, and FETs fabricated on these precisely diameter-controlled HACNT arrays exhibited a highest on/off current ratio approaching 10^7.

This E_{coh}-guided framework provides a direct link between catalyst thermodynamics, nanomaterial growth, and device-level functionality, offering causal evidence that synthesis-level diameter control enables reliable modulation of CNT-FET behavior. Beyond CNT growth, this interface-engineering approach suggests a general paradigm for regulating catalyst nanoparticle size in heterogeneous systems, where controlled dispersion and suppressed sintering are critical for functional performance. Such a descriptor-driven strategy may be broadly applicable to other catalyst-mediated nanostructure synthesis processes.

https://doi.org/10.1021/jacs.6c08950
J. Am. Chem. Soc. XXXX, XXX, XXX−XXX

4. METHODS

4.1. Support Treatment and Catalyst Implantation

A-plane sapphire sized 4 × 6 mm^2 (single-side polished, surface roughness <5 Å, miscut angle <0.5°, purchased from Hefei Kejing Materials Technology Co., Ltd.) was employed as the support substrate for HACNT array growth. Catalyst (Fe, Pt, or Ti) was implanted into the support by a FAD-MEVVA ion implanter at fluences of 1 × 10^{15} cm^{-2}, 1 × 10^{16} cm^{-2}, and 6 × 10^{15} cm^{-2} for different catalysts, and the implantation energy was set to 9 keV.

After implantation, the support was ultrasonically cleaned sequentially in deionized water, acetone, ethanol, and deionized water for 10, 15, 10, and 10 min, respectively, to remove surface contaminants. Subsequently, the support was annealed at 1100 °C for 8 h in air to repair lattice damage induced by ion implantation.

4.2. HACNT Growth via S-Apphire Strategy

A Y-shaped quartz tube served as the reactor for both sulfur modification and growth of HACNT arrays. The pristine sapphire support was positioned downstream of the Y junction within the central zone of the furnace (Thermo Co., Ltd.). One of the upstream arms (side arm) of the Y-shaped tube was dedicated to sulfur vapor generation, where sulfur powder was heated by using a heating tape. This arm was connected to an Ar gas source, which acts as the carrier gas of the sulfur vapor. The other upstream arms (main arm) supplied a mixture of Ar, H_2, and ethanol vapor (carried by Ar) for HACNT array growth.

The reactor was first purged with Ar while the furnace temperature was ramped to 800−900 °C and the sulfur source was heated to 120−140 °C within 30 min. Subsequently, 50 sccm of Ar was introduced through the sulfur branch to deliver sulfur vapor to the support region. Simultaneously, the sulfur source was cooled to room temperature and the sulfur branch was closed. H_2 (200−400 sccm) was introduced through the main branch for 5−10 min to promote catalyst diffusion to the surface and their aggregation into catalyst nanoparticles. Subsequently, ethanol vapor (10−30 sccm) was introduced as the carbon source, and HACNT arrays growth was carried out for 30 min.

4.3. DFT Calculation Details

Density functional theory (DFT) calculations were performed using the Vienna Ab initio Simulation Package (VASP) code.[43,44] The interactions between valence electrons and atomic cores were modeled using projector-augmented wave (PAW) pseudopotentials in combination with the Perdew−Burke−Ernzerhof (PBE) exchange-correlation functional.[45,46] A plane-wave basis set with a cutoff energy of 500 eV was employed. The convergence criteria for the energy and force were set to 10^{-5} eV and 0.03 eV $Å^{-1}$. From the bulk Al_2O_3 model, one Al atom was replaced by S, according to the experimental evidence. Then, the (1 1 0) surface models, namely Al_2O_3 or $Al_{2-x}O_3S_x$ surfaces, were cleaved to further study the metal-atom adsorption and diffusion. Brillouin zone sampling (K-point) was carried out using a Monkhorst−Pack mesh[47] of 1 × 3 × 1 for the 1 × 1 surface, and the Gamma point for the 1 × 2 surface. A dispersion correction was included using the DFT-D3 method.[48] The vacuum thickness along the z-direction was set to be 15 Å. The dipole correction was added. Although these are 0 K DFT total energies, they serve as universally accepted and highly reliable descriptors for high-temperature processes. Because the defined E_{coh} models a purely condensed-phase transition without high-entropy gas species, the inherently minor vibrational entropic contributions systematically cancel out when evaluating relative energetic trends across structurally similar systems.

4.4. Characterizations

SEM imaging was performed using a Hitachi S-8800 SEM operating at 1.0 kV and 15 μA. AFM imaging was obtained with a Bruker Dimension Icon system operating in ScanAsyst mode. XPS was performed on an AXIS Supra X-ray photoelectron spectrometer (Kratos Analytical Co., Ltd.) with Al K_α (1486.6 eV) as the X-ray source. XRD was operated on a D8 Advance instrument from Bruker AXS GmbH. Raman spectroscopy of the HACNT sample was carried out using a Jobin Yvon-Horiba LabRam system equipped with a Nikon × 100 objective lens (numerical aperture = 0.90).

For the characterization of support, the atomic structures of sapphire were characterized by a cold-field emission transmission electron microscope (JEM-ARM300F2 GRAND ARM2) operating at 300 kV. The convergent semiangle for the incident probe was set at ≈30 mrad. The collection angle of ADF-STEM images ranged from 60 to 200 mrad. ADF-STEM images were filtered by Gaussian filters, and the positions of atomic columns were located by finding the local maxima of the filtered series. EELS was acquired using a Gatan GIF Quantum spectrometer with a dispersion of 0.15 eV $channel^{-1}$ and an energy resolution of approximately 0.3 eV. EELS data analysis was performed using Digital Micrograph software. We first denoised the EELS data using principal component analysis (PCA) in Digital Micrograph.

TOF-SIMS measurements were performed using a PHI nanoTOF II instrument (from ULVAC-PHI Inc., Japan) at the Beijing Institute of Technology. A $[Bi_3]^{2+}$ primary ion beam (30 kV acceleration voltage) was used for sample analysis, while an Ar^+ beam (3 kV acceleration voltage, 100 nA current) was used to provide simultaneous sputter etching to generate the depth profiles for different species. The analysis area was sized 20 × 20 μm^2, and the sputtering area was 400 × 400 μm^2.

For catalyst characterization, a Titan Themis Z spherical aberration-corrected transmission electron microscope (Thermo Fisher Scientific) was employed. During the observation, high-angle annular dark-field (HAADF) images (collection angle: 80−180 mrad) and EDS spectra were acquired.

4.5. Fabrication and Measurements of Electrical Devices

We fabricated top-gated FETs in this work. First, marks for lithography alignment were patterned by electron beam lithography (EBL), and a Ti/Au film of 5/50 nm thickness was deposited using electron beam evaporation (EBE), followed by a liftoff process. Second, the channel region of FETs was defined by EBL patterning and reactive ion etching (RIE) with O_2 plasma. Then, we employed EBL to pattern source and drain, along with pads connected to them for measurement, followed by the deposition of a 50 nm thick Pd film by EBE. A liftoff process was followed. After that, a HfO_2 film of 7 nm thickness was deposited by atomic layer deposition (ALD). Finally, the gate electrode and its connecting pad were patterned by EBL and a 70 nm thickness Pd film was deposited by EBE, followed by a liftoff process. The channel length (gate length) ranges from 200 nm to 1 μm, and the channel width is 1 μm.

To measure the CNT-FET performance, an Agilent B1500A Semiconductor Device Analyzer and a probe station (EPS) were used, and tests were conducted at room temperature.

■ ASSOCIATED CONTENT

Data Availability Statement

The data that support the findings of this study are available from the corresponding author upon reasonable request.

Supporting Information

The Supporting Information is available free of charge at https://pubs.acs.org/doi/10.1021/jacs.6c08950.

Additional DFT calculation details, experimental details, analysis of sulfur substitution and the active catalyst state, as well as comprehensive material characterizations and CNT-FET performances, including Supporting Notes 1−7, Figures S1−S24, and Tables S1−S8 (PDF)

https://doi.org/10.1021/jacs.6c08950
J. Am. Chem. Soc. XXXX, XXX, XXX−XXX

AUTHOR INFORMATION

Corresponding Authors

Liu Qian − *School of Materials Science and Engineering, Peking University, Beijing 100871, China;* orcid.org/0009-0004-3090-8404; Email: qianliu-cnc@pku.edu.cn

Xiaoxu Zhao − *School of Materials Science and Engineering, Peking University, Beijing 100871, China;* orcid.org/0000-0001-9746-3770; Email: xiaoxuzhao@pku.edu.cn

Jia Si − *Key Laboratory for the Physics and Chemistry of Nanodevices and Center for Carbon-Based Electronics, Department of Electronics, Peking University, Beijing 100871, China;* orcid.org/0000-0003-0737-4905; Email: sijia@pku.edu.cn

Jin Zhang − *Beijing National Laboratory for Molecular Sciences, College of Chemistry and Molecular Engineering and School of Materials Science and Engineering, Peking University, Beijing 100871, China;* orcid.org/0000-0003-3731-8859; Email: jinzhang@pku.edu.cn

Authors

Jianping Wang − *Beijing National Laboratory for Molecular Sciences, College of Chemistry and Molecular Engineering and School of Materials Science and Engineering, Peking University, Beijing 100871, China*

Zijian Wang − *School of Materials Science and Engineering, Peking University, Beijing 100871, China*

Chengyu Wang − *Key Laboratory for the Physics and Chemistry of Nanodevices and Center for Carbon-Based Electronics, Department of Electronics, Peking University, Beijing 100871, China*

Shurui Wang − *Beijing National Laboratory for Molecular Sciences, College of Chemistry and Molecular Engineering and School of Materials Science and Engineering, Peking University, Beijing 100871, China*

Yue Li − *School of Materials Science and Engineering, Peking University, Beijing 100871, China;* orcid.org/0000-0002-3972-0692

Zhe Liu − *Beijing National Laboratory for Molecular Sciences, College of Chemistry and Molecular Engineering and School of Materials Science and Engineering, Peking University, Beijing 100871, China*

Xinyi Cai − *Beijing National Laboratory for Molecular Sciences, College of Chemistry and Molecular Engineering, Peking University, Beijing 100871, China*

Complete contact information is available at: https://pubs.acs.org/10.1021/jacs.6c08950

Author Contributions

The manuscript was written through contributions of all authors. All authors have given approval to the final version of the manuscript.

Notes

The authors declare no competing financial interest.

ACKNOWLEDGMENTS

This work was financially supported by the Ministry of Science and Technology of China (2022YFA1203302 and 2022YFA1203304), the National Natural Science Foundation of China (Grant Nos. 52021006, 22494641, and 52102032), the Beijing National Laboratory for Molecular Sciences (BNLMS-CXTD-202001), and the Shenzhen Science and Technology Innovation Commission (KQTD20221101115627004).

REFERENCES

(1) Haruta, M. Size- and support-dependency in the catalysis of gold. *Catal. Today* **1997**, *36* (1), 153−166.

(2) Qiao, B.; Wang, A.; Yang, X.; Allard, L. F.; Jiang, Z.; Cui, Y.; Liu, J.; Li, J.; Zhang, T. Single-atom catalysis of CO oxidation using Pt1/FeOx. *Nat. Chem* **2011**, *3* (8), 634−641.

(3) Wang, A.; Li, J.; Zhang, T. Heterogeneous single-atom catalysis. *Nat. Rev. Chem* **2018**, *2* (6), 65−81.

(4) Kaiser, S. K.; Chen, Z.; Faust Akl, D.; Mitchell, S.; Pérez-Ramírez, J. Single-Atom Catalysts across the Periodic Table. *Chem. Rev* **2020**, *120* (21), 11703−11809.

(5) Somorjai, G. A.; Park, J. Y. Molecular Factors of Catalytic Selectivity. *Angew. Chem. Int. Ed* **2008**, *47* (48), 9212−9228.

(6) Chen, X.; Qin, X.; Jiao, Y.; Peng, M.; Diao, J.; Ren, P.; Li, C.; Xiao, D.; Wen, X.; Jiang, Z.; et al. Structure-dependence and metal-dependence on atomically dispersed Ir catalysts for efficient n-butane dehydrogenation. *Nat. Commun* **2023**, *14* (1), 2588.

(7) Tauster, S. J.; Fung, S. C.; Baker, R. T. K.; Horsley, J. A. Strong Interactions in Supported-Metal Catalysts. *Science* **1981**, *211* (4487), 1121−1125.

(8) Wang, T.; Hu, J.; Ouyang, R.; Wang, Y.; Huang, Y.; Hu, S.; Li, W.-X. Nature of metal-support interaction for metal catalysts on oxide supports. *Science* **2024**, *386* (6724), 915−920.

(9) Hu, S.; Li, W.-X. Sabatier principle of metal-support interaction for design of ultrastable metal nanocatalysts. *Science* **2021**, *374* (6573), 1360−1365.

(10) Liu, L.; Han, J.; Xu, L.; Zhou, J.; Zhao, C.; Ding, S.; Shi, H.; Xiao, M.; Ding, L.; Ma, Z.; et al. Aligned, high-density semiconducting carbon nanotube arrays for high-performance electronics. *Science* **2020**, *368* (6493), 850−856.

(11) Ze, Y.; Liu, Y.; Wang, B.; Yin, H.; Jin, C.; Zhang, Z. Carbon nanotube materials for future integrated circuit applications. *Mater. Today* **2024**, *79*, 97−111.

(12) Ponce, F. A.; Bour, D. P. Nitride-based semiconductors for blue and green light-emitting devices. *Nature* **1997**, *386* (6623), 351−359.

(13) Matsuda, Y.; Tahir-Kheli, J.; Goddard, W. A., III Definitive Band Gaps for Single-Wall Carbon Nanotubes. *J. Phys. Chem. Lett* **2010**, *1* (19), 2946−2950.

(14) Hu, Y.; Kang, L.; Zhao, Q.; Zhong, H.; Zhang, S.; Yang, L.; Wang, Z.; Lin, J.; Li, Q.; Zhang, Z.; et al. Growth of high-density horizontally aligned SWNT arrays using Trojan catalysts. *Nat. Commun* **2015**, *6* (1), 6099.

(15) Xie, Y.; Li, Y.; Peng, Z.; Wang, C.; Qiu, Z.; Cai, X.; Song, T.; Si, J.; Zhao, X.; Qian, L.; et al. Nano-seeding catalysts for high-density arrays of horizontally aligned carbon nanotubes with wafer-scale uniformity. *Nat. Commun* **2025**, *16* (1), 149.

(16) Liu, Z.; Li, H.; Peng, Z.; Zou, M.; Yu, Z.; Li, Y.; Qiu, Z.; Sun, X.; Qian, L.; Zhang, J. Triggering Lattice Oxygen Release for Semiconducting Carbon Nanotube Array Synthesis. *J. Am. Chem. Soc* **2025**, *147* (36), 32752−32760.

(17) Javey, A.; Tu, R.; Farmer, D. B.; Guo, J.; Gordon, R. G.; Dai, H. High Performance n-Type Carbon Nanotube Field-Effect Transistors with Chemically Doped Contacts. *Nano Lett* **2005**, *5* (2), 345−348.

(18) Najari, M.; Frégonèse, S.; Maneux, C.; Mnif, H.; Masmoudi, N.; Zimmer, T. Schottky Barrier Carbon Nanotube Transistor: Compact Modeling, Scaling Study, and Circuit Design Applications. *IEEE Trans. Electron. Devices* **2011**, *58* (1), 195−205.

(19) Yoshida, H.; Takeda, S.; Uchiyama, T.; Kohno, H.; Homma, Y. Atomic-scale in-situ observation of carbon nanotube growth from solid state iron carbide nanoparticles. *Nano Lett* **2008**, *8* (7), 2082−2086.

(20) Chen, G.; Seki, Y.; Kimura, H.; Sakurai, S.; Yumura, M.; Hata, K.; Futaba, D. N. Diameter control of single-walled carbon nanotube forests from 1.3−3.0 nm by arc plasma deposition. *Sci. Rep* **2014**, *4* (1), 3804.

(21) Li, M.; Yang, F.; Ding, L.; Liu, X.; Zhang, Z.; Zhang, D.; Zhao, X.; Yang, J.; Li, Y. Diameter-specific growth of single-walled carbon nanotubes using tungsten supported nickel catalysts. *Carbon* **2017**, *118*, 485−492.
(22) Chiang, W.-H.; Mohan Sankaran, R. Linking catalyst composition to chirality distributions of as-grown single-walled carbon nanotubes by tuning NixFe1−x nanoparticles. *Nat. Mater* **2009**, *8* (11), 882−886.
(23) Ago, H.; Imamoto, K.; Ishigami, N.; Ohdo, R.; Ikeda, K.-i.; Tsuji, M. Competition and cooperation between lattice-oriented growth and step-templated growth of aligned carbon nanotubes on sapphire. *Appl. Phys. Lett* **2007**, *90*, 123112.
(24) Yin, P.; Luo, X.; Ma, Y.; Chu, S.-Q.; Chen, S.; Zheng, X.; Lu, J.; Wu, X.-J.; Liang, H.-W. Sulfur stabilizing metal nanoclusters on carbon at high temperatures. *Nat. Commun* **2021**, *12* (1), 3135.
(25) Yang, C.-L.; Wang, L.-N.; Yin, P.; Liu, J.; Chen, M.-X.; Yan, Q.-Q.; Wang, Z.-S.; Xu, S.-L.; Chu, S.-Q.; Cui, C.; et al. Sulfur-anchoring synthesis of platinum intermetallic nanoparticle catalysts for fuel cells. *Science* **2021**, *374* (6566), 459−464.
(26) Manzeli, S.; Ovchinnikov, D.; Pasquier, D.; Yazyev, O. V.; Kis, A. 2D transition metal dichalcogenides. *Nat. Rev. Mater* **2017**, *2* (8), 17033.
(27) Li, L.; Wang, Q.; Wu, F.; Xu, Q.; Tian, J.; Huang, Z.; Wang, Q.; Zhao, X.; Zhang, Q.; Fan, Q.; et al. Epitaxy of wafer-scale single-crystal MoS2 monolayer via buffer layer control. *Nat. Commun* **2024**, *15* (1), 1825.
(28) Zhang, W.; Fu, Q.; Luo, Q.; Sheng, L.; Yang, J. Understanding Single-Atom Catalysis in View of Theory. *JACS Au* **2021**, *1* (12), 2130−2145.
(29) Yang, X.; Song, W.; Liao, K.; Wang, X.; Wang, X.; Zhang, J.; Wang, H.; Chen, Y.; Yan, N.; Han, X.; et al. Cohesive energy discrepancy drives the fabrication of multimetallic atomically dispersed materials for hydrogen evolution reaction. *Nat. Commun* **2024**, *15* (1), 8216.
(30) He, M.; Zhang, S.; Zhang, J. Horizontal Single-Walled Carbon Nanotube Arrays: Controlled Synthesis, Characterizations, and Applications. *Chem. Rev* **2020**, *120* (22), 12592−12684.
(31) Jorio, A.; Saito, R.; Hafner, J. H.; Lieber, C. M.; Hunter, M.; McClure, T.; Dresselhaus, G.; Dresselhaus, M. S. Structural (n,m) Determination of Isolated Single-Wall Carbon Nanotubes by Resonant Raman Scattering. *Phys. Rev. Lett* **2001**, *86* (6), 1118−1121.
(32) Liu, K.; Wang, W.; Wu, M.; Xiao, F.; Hong, X.; Aloni, S.; Bai, X.; Wang, E.; Wang, F. Intrinsic radial breathing oscillation in suspended single-walled carbon nanotubes. *Phys. Rev. B* **2011**, *83* (11), 113404.
(33) Sodhi, R. N. S. Time-of-flight secondary ion mass spectrometry (TOF-SIMS): –versatility in chemical and imaging surface analysis. *Analyst* **2004**, *129* (6), 483−487.
(34) Song, T.; Zou, M.; Lu, D.; Chen, H.; Wang, B.; Wang, S.; Xu, F. Probing Surface Information of Alloy by Time of Flight-Secondary Ion Mass Spectrometer. *Crystals* **2021**, *11* (12), 1465.
(35) Costa, T.; Santos, S.; Silva, C.; Neto, E.; Pereira, C.; Freitas, N. Microstructure and morphology of mechanically sulfated acid catalysts of α-Al2O3. *Cerâmica* **2021**, *67*, 308−315.
(36) Bristow, J. K.; Tiana, D.; Parker, S. C.; Walsh, A. Defect chemistry of Ti and Fe impurities and aggregates in Al2O3. *J. Mater. Chem. A* **2014**, *2* (17), 6198−6208.
(37) Hunault, M. O. J. Y.; Harada, Y.; Miyawaki, J.; Wang, J.; Meijerink, A.; de Groot, F. M. F.; van Schooneveld, M. M. Direct Observation of Cr3+ 3d States in Ruby: Toward Experimental Mechanistic Evidence of Metal Chemistry. *J. Phys. Chem. A* **2018**, *122* (18), 4399−4413.
(38) Smirnov, M. Y.; Kalinkin, A. V.; Pashis, A. V.; Sorokin, A. M.; Noskov, A. S.; Kharas, K. C.; Bukhtiyarov, V. I. Interaction of Al2O3 and CeO2 Surfaces with SO2 and SO2 + O2 Studied by X-ray Photoelectron Spectroscopy. *J. Phys. Chem. B* **2005**, *109* (23), 11712−11719.
(39) Ou, S.; Heimann, J. E.; Bennett, J. W. A Density Functional Theory (DFT) Investigation of Sulfur-Based Adsorbate Interactions on Alumina and Calcite Surfaces. *Clays Clay Miner.* **2022**, *70* (3), 370−385.
(40) Xie, Y.; Qian, L.; Lin, D.; Yu, Y.; Wang, S.; Zhang, J. Growth of Homogeneous High-Density Horizontal SWNT Arrays on Sapphire through a Magnesium-Assisted Catalyst Anchoring Strategy. *Angew. Chem. Int. Ed* **2021**, *60* (17), 9330−9333.
(41) Jozwiak, W. K.; Kaczmarek, E.; Maniecki, T. P.; Ignaczak, W.; Maniukiewicz, W. Reduction behavior of iron oxides in hydrogen and carbon monoxide atmospheres. *Appl. Catal., A* **2007**, *326* (1), 17−27.
(42) Cao, Q.; Rogers, J. A. Ultrathin Films of Single-Walled Carbon Nanotubes for Electronics and Sensors: A Review of Fundamental and Applied Aspects. *Adv. Mater* **2009**, *21* (1), 29−53.
(43) Kresse, G.; Joubert, D. From ultrasoft pseudopotentials to the projector augmented-wave method. *Phys. Rev. B* **1999**, *59* (3), 1758−1775.
(44) Kresse, G.; Furthmüller, J. Efficient iterative schemes for ab initio total-energy calculations using a plane-wave basis set. *Phys. Rev. B* **1996**, *54* (16), 11169−11186.
(45) Blöchl, P. E. Projector augmented-wave method. *Phys. Rev. B* **1994**, *50* (24), 17953−17979.
(46) Perdew, J. P.; Burke, K.; Ernzerhof, M. Generalized Gradient Approximation Made Simple. *Phys. Rev. Lett* **1996**, *77* (18), 3865−3868.
(47) Monkhorst, H. J.; Pack, J. D. Special points for Brillouin-zone integrations. *Phys. Rev. B* **1976**, *13* (12), 5188−5192.
(48) Grimme, S.; Antony, J.; Ehrlich, S.; Krieg, H. A consistent and accurate ab initio parametrization of density functional dispersion correction (DFT-D) for the 94 elements H-Pu. *J. Chem. Phys* **2010**, *132* (15), 154104.

https://doi.org/10.1021/jacs.6c08950
J. Am. Chem. Soc. XXXX, XXX, XXX−XXX